Geometric deep learning-based coronary wall shear stress estimation from real-world patients

Computers in Biology and Medicine 205 (2026) 111583

Contents lists available at ScienceDirect

Computers in Biology and Medicine

journal homepage: www.elsevier.com/locate/compbiomed

Geometric deep learning-based coronary wall shear stress estimation from real-world patients

Bianca Griffo [a,b], Diego Gallo [a,b], David Marlevi [c,d], Marco Laudato [e], Girolamo Mastronuzzi [a,b], Claudio Chiastra [a,b], Alessandro Candreva [f], Carlos Collet [g,h,i], Bernard De Bruyne [g,j], Andrea Erriquez [k], Gianluca Campo [k], Simone Biscaglia [k], Umberto Morbiducci [a,b], Maurizio Lodi Rizzini [a,b,*]

[a] Department of Mechanical and Aerospace Engineering, Politecnico di Torino, Turin, Italy
[b] PolitoBIOMed Lab, Politecnico di Torino, Turin, Italy
[c] Department of Molecular Medicine and Surgery, Karolinska Institute, Solna, Sweden
[d] Institute for Medical Engineering and Sciences, Massachusetts Institute of Technology, Cambridge, MA, United States
[e] FLOW Research Center, Department of Engineering Mechanics, KTH Royal Institute of Technology, Stockholm, Sweden
[f] Department of Cardiology, Zurich University Hospital, Zurich, Switzerland
[g] Cardiovascular Center Aalst, OLV-Clinic, Aalst, Belgium
[h] Division of Cardiology, New York Presbyterian Hospital Columbia University, NY, New York, United States
[i] Clinical Trial Center, Cardiovascular Research Foundation, New York, NY, United States
[j] Department of Cardiology, University Hospital of Lausanne, Lausanne, Switzerland
[k] Cardiology Unit, Azienda Ospedaliero Universitaria di Ferrara, Cona (FE), Italy

ARTICLE INFO

Keywords:
Coronary artery disease
Wall shear stress
Geometric deep learning

ABSTRACT

Background: Coronary wall shear stress (WSS) derived from computational fluid dynamics (CFD) provides mechanistic insight and prognostic information, but its clinical translation is hindered by modeling complexity and computation time. We evaluated a geometric deep learning framework based on gauge-equivariant mesh graph convolutional network (GEM-GCN) to estimate coronary WSS directly in geometries reconstructed from coronary angiography in real-world patients.

Methods: A total of 1078 coronary arteries from 748 patients were reconstructed from invasive angiography. Time-averaged WSS computed by transient CFD served as reference labels for GEM-GCN training and testing. Two experiments were conducted: (i) random splitting of the full dataset with 10-fold cross-validation, and (ii) a *clinical split*, to assess whether GEM-GCN–derived WSS preserved the ability to predict myocardial infarction (MI) compared with CFD-derived WSS.

Results: GEM-GCN produced patient-specific WSS maps in < 5s per vessel. GEM-GCN slightly underestimated lesion- and vessel-averaged WSS in the random split, with absolute and percentage errors equal to 0.48 [0.26–0.78] Pa and 23.6 [14.8–42.6]%, respectively. High spatial agreement was found for high-WSS regions (Dice distance 0.88 [0.81–0.92]). Similar performance was observed in the *clinical split* (absolute error 0.65 [0.41–1.12] Pa; Dice distance 0.84 [0.71–0.90]). After normalization by vessel-averaged WSS, the correlation between GEM-GCN-derived and CFD lesion-averaged WSS improved from $R = 0.67$ to $R = 0.89$ ($p < 0.0001$). Lesion-averaged WSS and the lesion-to-vessel WSS ratio achieved comparable MI prediction performance for CFD and GEM-GCN.

Conclusions: Geometric deep learning enables fast, CFD-free coronary WSS estimation from routine angiography, supporting its potential for large-scale, real-world risk stratification.

* Corresponding author. PolitoBIOMed Lab Department of Mechanical and Aerospace Engineering Politecnico di Torino Corso Duca degli Abruzzi, 24, 10129, Turin, Italy.
E-mail address: maurizio.lodirizzini@polito.it (M. Lodi Rizzini).

https://doi.org/10.1016/j.compbiomed.2026.111583
Received 12 December 2025; Received in revised form 4 February 2026; Accepted 21 February 2026
Available online 25 February 2026

1. Introduction

Coronary artery disease (CAD) remains the leading cause of mortality worldwide, with myocardial infarction (MI) representing its most severe clinical manifestation [1]. The primary pathological mechanisms underlying acute coronary syndromes are the rupture and erosion of atherosclerotic plaques [2,3]. Near-wall hemodynamics features, particularly wall shear stress (WSS) patterns, play a central role in this context. Acting directly on the endothelium, WSS is recognized as a key factor in the initiation, progression and destabilization of atherosclerotic plaques [3–8]. In particular, elevated WSS in diseased coronary arteries has been associated with plaque rupture and erosion, and consequently with an increased risk of MI [2,6,8,9].

Computational fluid dynamics (CFD) enables the quantitative assessment of coronary hemodynamics by providing patient-specific calculations of WSS within image-based, three-dimensional (3D) models [10–13]. Despite its strong potential for clinical applications such as MI risk prediction [6,8,9,14], the widespread adoption of personalized CFD simulations remains limited by their high computational cost and by the need for adequate expertise or specialized training [10,11,15]. To overcome this limitation, recent studies have explored the use of artificial intelligence (AI)-based surrogate models as faster alternatives to CFD, aiming to provide clinically feasible WSS estimates. Efforts to achieve affordable AI-based WSS predictions have been recently reported across several vascular beds [16]. Among the various AI-based strategies, deep learning (DL) techniques have gained momentum for reducing computational demands while predicting accurate WSS measures in coronary arteries. These approaches can generally be classified into four main categories: (i) fully-connected, convolutional neural networks (CNNs) or generative adversarial networks (GANs) applied to one or two-dimensional (2D) parametrizations of the 3D coronary wall [17–20]; (ii) point cloud-based networks, operating directly on 3D point-cloud representations of the vessel geometry [21]; (iii) mesh-based methods, leveraging a graph representation of the arterial surface mesh [22]; (iv) transformers-based architectures [23]. Although all the reported approaches have all yielded promising results, with average approximation errors in the range 5.5% - 11.7% and normalized errors in the range 0.5% - 6% (a summary of the findings and the adopted datasets of these studies is reported in Table 1), almost the totality of them have been applied primarily to idealized or synthetically generated 3D models of coronary arteries [17–23]. Their application to real-world datasets remains limited, mainly due to the scarce availability of large datasets of patient-specific coronary models required for training AI-based models. Specifically, Suk et al. [22] achieved a median approximation error under 8%. In this work, we aim to predict WSS on the luminal surface of patient-specific coronary artery geometries reconstructed from 3D quantitative coronary angiography (3D-QCA) exploiting DL and evaluating the agreement with WSS computed from traditional CFD simulations. To do that, we extend a previously proposed geometric DL mesh-based strategy [22] from idealized to patient-specific coronary arteries. By applying this approach to a large dataset of real-world patients, we demonstrate the potential of DL to substantially reduce the computational time required for a personalized and reliable WSS estimation, thereby supporting its translation into a practical clinical biomarker for CAD diagnosis and management. Additionally, we tested whether the predictive capacity of DL-derived WSS for MI at 5 years was preserved relative to that of CFD-derived WSS.

Table 1
Representative studies employing artificial intelligence for coronary WSS prediction.

Study	Method	Error (mean)	Dataset
Su et al. [17]	MLR; MLP; CNN	NMAE 2.5%, AE 11.7%	2000 idealized vessels
Gharleghi et al. [18]	CNN	$NMAE_{peak}$ 0.24%, $NMAE_{mean}$ 4.2%	2753 vessels (127 patient-specific + 2626 synthetically generated)
Alamir et al. [19]	CNN	$NMAE_{max-min}$ 6.03%	600 (50 patient-specific vessels + 550 synthetically generated)
Nikpour & Mohebbi [20]	cGAN	$NMAE_{max-min}$ 0.6%, $NMAE_{peak}$ 1.08%	1400 (350 patient-specific vessels + 1050 synthetically generated)
Sarkhosh et al. [21]	CNN	$NMAE_{max-min}$ 2.5%, MRE 11.3%	1800 idealized vessels
Suk et al. [22]	GEM-GCN	$NMAE_{peak}$ 0.5%, AE 7.8%	2000 idealized single vessels 2000 idealized bifurcating vessels
Suk et al. [23]	GATr	AE 5.5%	2000 idealized single vessels 2000 idealized bifurcating vessels

Nomenclature: CNN: Convolutional neural network, MLP: Multi-layer perceptron, MLR: Multi-linear regression, AE: approximation error; NMAE: normalized mean absolute error ($NMAE_{peak}$: normalized by peak, $NMAE_{mean}$: normalized by mean; $NMAE_{max-min}$: normalized by maximum – minimum); MRE: Mean radial error, cGAN: Conditional generative adversarial network; GEM-GCN: Gauge equivariant mesh graph convolutional network; GATr: Geometric algebra transformer.

2. Materials and methods

2.1. Data collection

A total of 1078 coronary arteries from 748 patients were analyzed, including single-branch segments of left anterior descending (LAD), left circumflex (LCX), and right coronary artery (RCA). The dataset was assembled from data collected from three previous clinical studies [8, 24–26]. Details of the anatomical characteristics for the total dataset and the three data subsets are reported in Table 2, while patient inclusion/exclusion criteria, and demographic and clinical details, which have already been extensively reported elsewhere [8,24,25], are summarized in the Supplementary Material.

The first subset comprised 520 diseased coronary arteries (333 patients) from the Fractional Flow Reserve versus Angiography for Multivessel Evaluation 2 (FAME 2) trial [24]. The second subset included 371 diseased coronary arteries (335 patients) from the Functional Assessment in Elderly MI Patients With Multivessel Disease (FIRE) trial [25,26]. The third subset consisted of 187 coronary arteries (80 patients) obtained from a multicenter study ("*future culprit" study*) [8]. Two data splits were implemented. First, the whole dataset, obtained merging vessels from all three subsets, was employed for training, validation and test purposes of the employed DL model to evaluate model accuracy (namely, random split). Additionally, a second split (namely, *clinical split*) was implemented by conducting training and validation on the 891

Table 2
Overview of coronary vessel types and percentage area stenosis across the three data subsets employed for this study. Percentage area stenosis is reported as median [interquartile range (IQR)].

		FAME 2 dataset (N = 520)	FIRE dataset (N = 371)	*Future culprit* dataset (N = 187)	Entire dataset (N = 1078)
Coronary vessel	LAD, no. (%)	225 (43.3%)	120 (32.3%)	69 (36.9%)	414 (38.4%)
	LCX, no. (%)	130 (25.0%)	137 (36.9%)	66 (35.3%)	333 (30.9%)
	RCA, no. (%)	165 (31.7%)	114 (30.7%)	52 (27.8%)	331 (30.7%)
Percentage area stenosis	/	61.7 [51.5-74.8]%	56.8 [47.9-65.4]%	51.3 [41.5-61.7]%	58.5 [48.3-68.4]%

diseased coronary arteries derived from the FIRE and FAME 2 dataset, while the third subset was used only for testing purposes, to (i) perform an external validation, and (ii) assess the clinical relevance of the employed geometric DL-based approach. In the third data subset, included patients experienced an MI and had undergone coronary angiography between 1 month and 5 years before the event (median time 25.9 months, interquartile range 21.9–29.8) [8]. Additional inclusion criteria were: (i) presence of a mild atherosclerotic lesion (≤50% diameter reduction on angiography) that was subsequently identified as the culprit for MI, and (ii) presence of at least one additional non-culprit lesion in one of the other two major epicardial coronary arteries [8]. Among the 187 vessels, 80 presented a future culprit lesion (FCL) and 107 presented a non-culprit lesion (NCL). All three studies were conducted in accordance with the ethical principles of the 1975 Declaration of Helsinki, with protocols approved by the respective institutional ethics committees. Written informed consent was obtained from all the enrolled patients.

2.2. 3D vessel reconstruction and lesion identification

The study workflow is illustrated in Fig. 1. Vessel geometries were reconstructed from two angiographic projections separated by at least 30° using 3D-QCA (CAAS Workstation WSS software, Pie Medical Imaging, Maastricht, the Netherlands), as previously described [8,27]. Within each reconstructed coronary model, the lesion segment (LS) was defined as the vessel region encompassing the minimum lumen area (MLA), as shown in Fig. 2. The proximal and distal boundaries of this segment were automatically determined at the intersections between the 3D-QCA lumen area line and the interpolated line of reference vessel area [8,27].

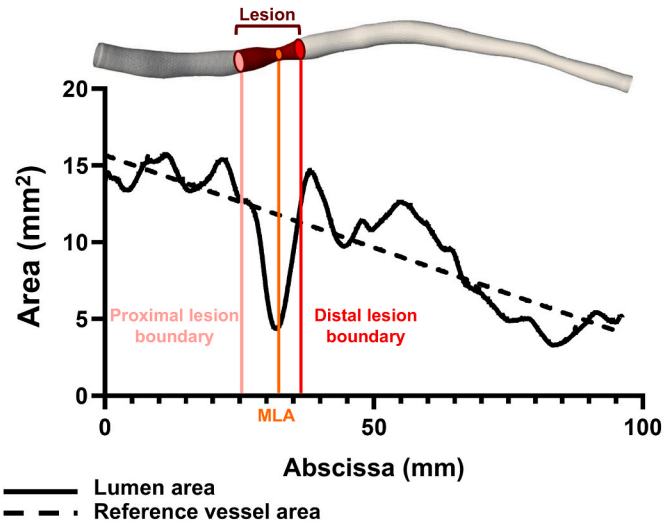

Fig. 2. Anatomical identification of the lesion segment based on 3D-QCA according to clinical practice. The trend of the luminal cross-sectional area as function of the abscissa is shown with reference vessel area (dashed line). The minimum lumen cross-sectional area, distal and proximal edges defining the LS are also highlighted. The LS is also graphically represented on the surface of one explanatory LAD model of the cohort under study.

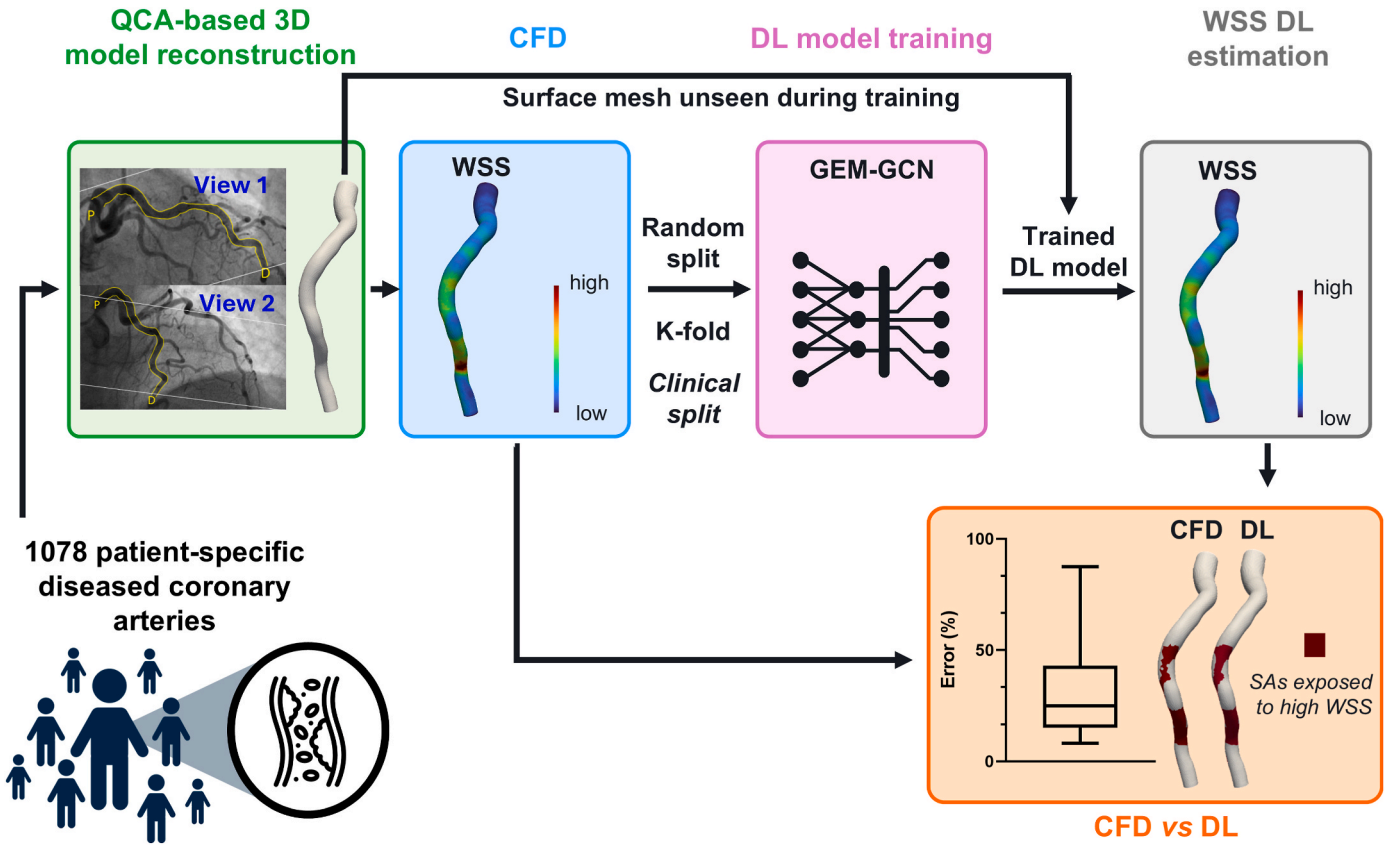

Fig. 1. Study workflow. A dataset of 1078 patient-specific diseased coronary arteries were considered for this study derived from three different clinical studies [8,24,25]. The 3D models of the vessels were reconstructed from 3D-QCA and then CFD simulations were performed to obtain the WSS vector field. The whole dataset was subdivided either with a random split or with a k-fold split into training (80%), validation (10%) and test (10%) sets. A *clinical split* was also performed by holding-out as test set only the subset comprised of 187 vessels derived from Ref. [8]. The adopted DL model, based on GEM-GCNs [22,30], was then fed with the samples. Once trained, the DL model was fed with the samples of the held-out test set and the WSS estimation was obtained. Finally, luminal SAs exposed to high WSS values were identified on both CFD and DL WSS distribution with vessel-specific thresholds defined by the 80th percentile of WSS magnitude distribution.

2.3. Computational hemodynamics

WSS was computed from transient CFD simulations, solving the governing equations of fluid motion with the clinical finite element-based software package CAAS Workstation WSS software. Meshing and simulation settings in the software used here represent a trade-off between computational time and accuracy and have been validated against traditional CFD simulations in a previous work [8]. Blood was modeled as an incompressible, homogeneous, Newtonian fluid with a density of 1060 kg/m^3 and dynamic viscosity of 0.0035 Pa·s. Concerning inlet boundary condition, a vessel-specific flow rate waveform, scaled to the individual vessel according to a diameter-based scaling law [28], was applied for each major epicardial artery (LAD, LCX, and RCA) [8]. Each scaled waveform was then imposed at the inflow section in terms of parabolic velocity profile [29]. As for the boundary condition at the outflow boundary, a constant reference pressure was prescribed. Vessel walls were assumed rigid, with a no-slip condition applied.

Additional information on the fluid domain discretization and CFD simulation settings is available elsewhere [8].

2.4. Graph neural networks for coronary hemodynamics estimation

The approach adopted here builds on a previously proposed mesh-based strategy [22] that employed gauge-equivariant mesh graph convolutional networks (GEM-GCNs) [30] implemented in PyTorch, in combination with the PyTorch Geometric library [22]. In this framework, the coronary artery wall is represented as a 2D manifold, corresponding to the same surface mesh used in the CFD simulations. Graph neural networks (GNNs) were applied by encoding the mesh topology into a graph structure $G = (V,E)$, where the coordinates of the generic vertex $v_p \in V$ (corresponding to the mesh nodes) are defined in $\mathbb{R}^3$, and edges e_{pq} connect adjacent nodes v_p and v_q [22]. In detail, the implemented GNN follows an encoder–decoder architecture that takes as input a vector field of features $x^{in} : V \to \mathbb{R}^{c_{in}}$, where c_{in} is the vector size, and outputs an estimated vector field $x^{out} : V \to \mathbb{R}^{c_{out}}$ (*i.e.,* WSS) of size c_{out}, associated with the same vertices of the input graph, leveraging graph latent representations [22]. The GEM-GCN employed in this study is composed of multiple building blocks, including specific operations and layers, outlined in Fig. 3 and described below.

Technically, the architecture comprises 14 residual blocks, each consisting of two convolutional layers and one skip connection to

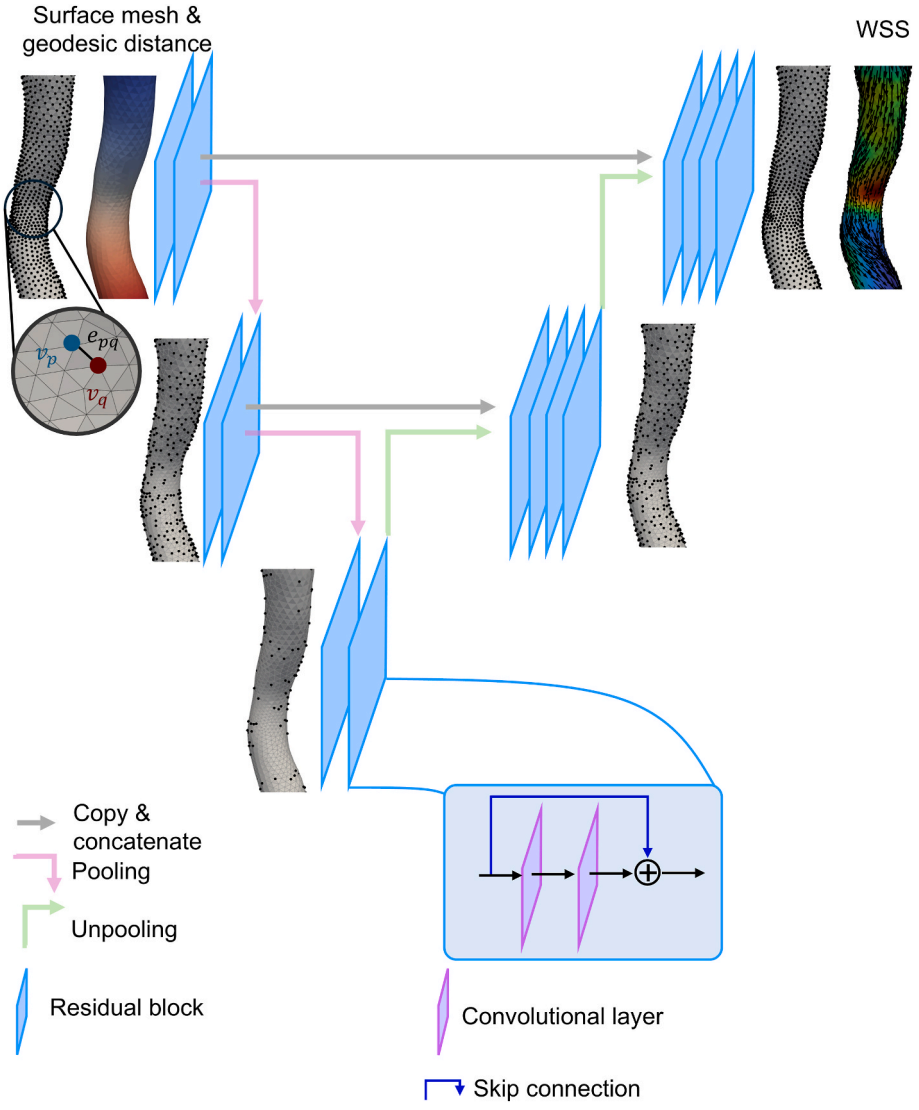

Fig. 3. Schematic illustration of the exploited neural network, based on the previously proposed network in Ref. [22]. The network obtained stacking residual blocks and pooling/unpooling layers takes as input the artery surface mesh together with the geodesic distance from the vessel inlet and outputs the corresponding WSS vector field.

mitigate issues related to vanishing gradients [31]. Let $x : V \rightarrow \mathbb{R}^c$ denote the feature vector associated with each vertex, where c is the channel size, and let $X(V, \mathbb{R}^c)$ represent the set of all fields mapping the node set V to $\mathbb{R}^c$. Graph convolution is defined *via* a message passing operator M, parameterized by a kernel K ($K : V \times V \in \mathbb{R}^{c_i \times c_{i+1}}$, where c_i and c_{i+1} are the input and output channel sizes of the ith layer) [22,30,32]:

$$M(p,x) := \sum_{q \in N_r(p) \cap V} K(p,q)\rho(p,q)x(q) \quad (1)$$

In eq. (1), $\rho(p,q) \in \mathbb{R}^{c_i \times c_i}$ is an invertible aggregation matrix that performs parallel transport of signals across neighboring vertices along the manifold. In practice, this means that the signal vector x is transported from v_q to v_p while preserving a fixed orientation relative to the shortest geodesic curve. Thus, for vertex $v_p \epsilon V$, the information from all neighborhood vertices within a radius r, *i.e.*, $N_r(p) \cap V$, is aggregated. The kernel K is defined to be anisotropic, allowing the model to distinguish between vertices in the neighborhood based on their angular position. Moreover, K is designed to be equivariant to changes in the local basis [22,30]. This ensures that GEM convolution can be implemented together with the representation of vector x in terms of the irreducible representations of the planar rotation symmetry group SO(2) [22,30]. Technically, the convolutional filter acts on the local tangent plane at each surface point, thereby approximating both the surface and its neighborhood projected onto that plane. Features are then parallel transported along the manifold for aggregation. Since the choice of a tangent plane (gauge) on a manifold is inherently arbitrary [30,33], gauge-equivariant message passing is performed in combination with parallel transport. This ensures that convolution outcomes are gauge equivariant to local coordinate system choices, as detailed in previous studies [30]. Finally, the output of the convolution operation is defined through the update function σ:

$$(M^*x) := \sigma(M(p,x)) \; \forall v_p \in V, \quad (2)$$

with $(M^*x) : X(V, \mathbb{R}^{c_i}) \rightarrow X(V, \mathbb{R}^{c_{i+1}})$.

The network also includes two pooling layers, which act on the vertex set $V = V_0$ of the input graph by hierarchically sampling it into smaller subsets $V_0 \supset V_1 \supset \cdots \supset V_n$. At each stage, disjoint vertex clusters C are formed using a nearest neighbor approach. Finally, for each vertex $v_p \in V_{i+1}$, per-vertex features of the corresponding cluster $C(p) \subset V_i$ are aggregated *via* parallel transport and then averaged through the pooling operator $\psi_{pool} : X(V_i, \mathbb{R}^c) \rightarrow X(V_{i+1}, \mathbb{R}^c)$ defined as follows:

$$\psi_{pool} := \frac{1}{|C(p)|} \sum_{q \in C(p)} \rho(p,q)x(q) \; \forall v_p \in V_{i+1}, \quad (3)$$

The corresponding unpooling operator $\psi_{unpool} : X(V_{i+1}, \mathbb{R}^c) \rightarrow X(V_i, \mathbb{R}^c)$ restores features from V_{i+1} back to V_i by applying parallel inverse transport, thus returning the coarsened node features back to the original vertices:

$$\psi_{unpool} := \rho^{-1}\left(C^{-1}(p), p\right)x\left(C^{-1}(p)\right) \; \forall v_p \in V_i, \quad (4)$$

where $C^{-1}(p)$ denotes the parent vertex in V_{i+1} associated with $v_p \in V_i$ [22,33].

Copy and concatenate operations are performed between matching layers in the contracting and expanding parts of the network, together with batch normalization and the application of Rectified Linear Unit (ReLU) activation function, defined as $a(x) = max(0, x)$ [34].

Further mathematical details regarding the network architecture and its operations are provided elsewhere [22,30]. The following subsection describes the input features, training strategy, and evaluation protocol adopted for the implemented DL model.

2.4.1. Node input features, training, and testing

The input features $x^{c_{in}}$ proposed in Ref. [22] were adopted in this study and are described below. These features were designed to ensure rotation equivariance and translation invariance of the input surface mesh. Specifically, for each vertex v_q in the local neighborhood of v_p, defined as $N_r(p) \cap V$, three matrices were obtained by computing (i) the outer product of the vector from v_p to v_q with itself, (ii) the outer product of the surface normal at v_q with itself, and (iii) the outer product between the vector from v_p to v_q and the surface normal at v_q. Then, each one of the resulting 3×3 matrices was averaged over the local neighborhood of v_p. These matrices capture meaningful local shape descriptors of the vessel. To include additional global information about flow direction, the three averaged matrices were concatenated with the shortest geodesic distance of each vertex v_p from the inflow surface, computed using the vector heat method [22,35].

The combination of rotation equivariant and translation invariant input features, together with the previously defined GEM convolution, pooling, and unpooling operators, enabled the construction of a fully SE(3)-equivariant model [22]. This property guarantees equivariance under both rotation and translation of the mesh in $\mathbb{R}^3$, which is particularly relevant given the absence of a canonical and unique coordinate system for the analyzed surface meshes [22,30].

The time-varying WSS, obtained from CFD simulations, was averaged over the cardiac cycle and used as the target physical quantity to be predicted by the GEM-GCN on the luminal vessel surface.

Model hyperparameters values were based on prior work [22], after confirming that both model depth and learning rate were suitable for the present cases. Training was then performed with these optimal settings on a single NVIDIA A30 GPU (24 GB) for up to 3000 epochs, based on model convergence and validation loss. The L1 loss function was employed due to its reduced sensitivity to outliers [22]. Moreover, Adam optimizer (learning rate equal to $1{\cdot}10^{-3}$) was employed, with a batch size of 4 to accommodate GPU memory constraints.

The above-described DL model was applied to perform two different independent experiments using two different data splits, *i.e.,* a random split and a *clinical split*. For the former experiment, the entire dataset of coronary artery models was randomly split into training (80%), validation (10%), and test (10%) sets, while preserving the relative distribution of vessels from the three original clinical studies across all sets. To assess the robustness of model's performance, specifically its independence from the training samples, 10-fold cross-validation was also performed.

Then, to assess the capacity of GEM-GCN-derived WSS to predict future MI events at 5 years, the DL-based approach was applied for the second experiment using a held-out test set (*clinical split*) consisting of the 187 (17%) coronary arteries from Ref. [8]. The remaining 891 arteries from Refs. [24,25] were used for training (69%) and validation (14%), preserving the relative distribution from the two original studies.

2.5. Performance evaluation and statistical analysis

The performance of the network was first evaluated in terms of absolute and percentage errors in the WSS magnitude obtained by the GEM-GCN ($\boldsymbol{WSS_{DL}}$) with respect to the CFD-derived reference values ($\boldsymbol{WSS_{CFD}}$):

$$Error\ (Pa) = |\boldsymbol{WSS_{CFD}} - \boldsymbol{WSS_{DL}}|, \quad (5)$$

$$Error\ (\%) = (|\boldsymbol{WSS_{CFD}} - \boldsymbol{WSS_{DL}}| \,/\, |\boldsymbol{WSS_{CFD}}|){\cdot}100 \quad (6)$$

In addition, the network's ability to identify luminal surface areas (SAs) exposed to high WSS magnitude values was assessed, given their pathological relevance. SAs were defined using vessel-specific thresholds corresponding to the 80th percentile of the WSS magnitude distribution, computed separately for the CFD (SA_{CFD}) and GEM-GCN (SA_{DL}) results. The co-localization between SA_{DL} and SA_{CFD} was then quantified using the Dice Distance (DD), defined as:

$$DD = \frac{2(SA_{CFD} \cap SA_{DL})}{SA_{CFD} + SA_{DL}}, 0 \leq DD \leq 1 \quad (7)$$

Furthermore, three additional metrics of clinical interest were computed: (i) lesion-averaged WSS, defined as the WSS magnitude spatially averaged over the lesion segment; (ii) vessel-averaged WSS, defined as the WSS spatially averaged over the entire vessel; and (iii) lesion-to-vessel WSS ratio, obtained as the ratio between the previous quantities. These metrics were evaluated for both the CFD-derived (reference) and GEM-GCN-predicted WSS magnitudes to enable direct comparison in both the random split and *clinical split*. To better understand how geometric complexity influences GEM-GCN performance the metrics evaluated to assess GEM-GCN performance in the held-out test set obtained by randomly splitting the dataset (namely, absolute and percentage errors, DD) were correlated with canonical centerline-based attributes representative of real-world vessels complexity as extensively reported in the Supplementary Material. Moreover, to assess the impact of stenosis severity on GEM-GCN performance, both the training set and the held-out test set obtained with the random split were stratified into 3 subgroups based on the main lesion severity, quantified *via* %AS, as described in detail in the Supplementary Material.

Continuous variables are reported as median [IQR]. The Kruskal-Wallis statistical test was used to assess differences in continuous variables across folds in the 10-fold cross-validation. The discriminative ability of WSS to predict future MI was evaluated using C-statistics. Receiver operator characteristics (ROC) curves were analyzed in terms of area under the curve (AUC). Comparisons between AUCs were performed using the DeLong test [36]. All analyses were conducted in R statistical software (version 4.4.1, R Foundation for Statistical Computing, Vienna, Austria), with a significance threshold of $p < 0.05$.

3. Results

3.1. Random split and 10-fold cross validation analysis

The average time required to obtain GEM-GCN-predicted WSS per coronary artery was 2.95 ± 1.15 s.

Fig. 4A presents the CFD-derived and GEM-GCN-predicted WSS magnitudes, along with their corresponding error distributions on the luminal surface, for two representative coronary artery models from the test set obtained through random data splitting of the entire dataset, *i.e.*, the best-performing case (DD = 0.98) and the worst-performing case (DD = 0.33). The corresponding SAs exposed to high WSS magnitude for these vessels are shown in Fig. 4B. The overall distribution of surface-averaged WSS magnitude errors across the test set is shown in Fig. 4C, reported as both absolute error (0.48 [0.26-0.78] Pa) and percentage error (23.55 [14.81-42.62] %). These results reveal local discrepancies between CFD-derived and GEM-GCN-predicted WSS magnitudes. Conversely, the identification of SAs exposed to elevated WSS magnitude showed consistent localization between CFD and GEM-GCN predictions, with high DD values (0.88 [0.81-0.92], Fig. 4D). As reported in Fig. S1 and detailed in the Supplementary Material, all the metrics used to evaluate GEM-GCN performances resulted weakly correlated with vessel tortuosity.

Analysis of lesion-averaged WSS (Fig. 5, left panel, R = 0.67, $p < 0.0001$) and vessel-averaged WSS (Fig. 5, middle panel, R = 0.63, $p < 0.0001$) across the test-set vessels revealed discrepancies between CFD-derived and GEM-GCN-predicted WSS magnitudes. These findings are consistent with the observed error distributions, demonstrating a moderate yet significant linear correlation and indicating a systematic underestimation of WSS magnitude by the network. Notably, when

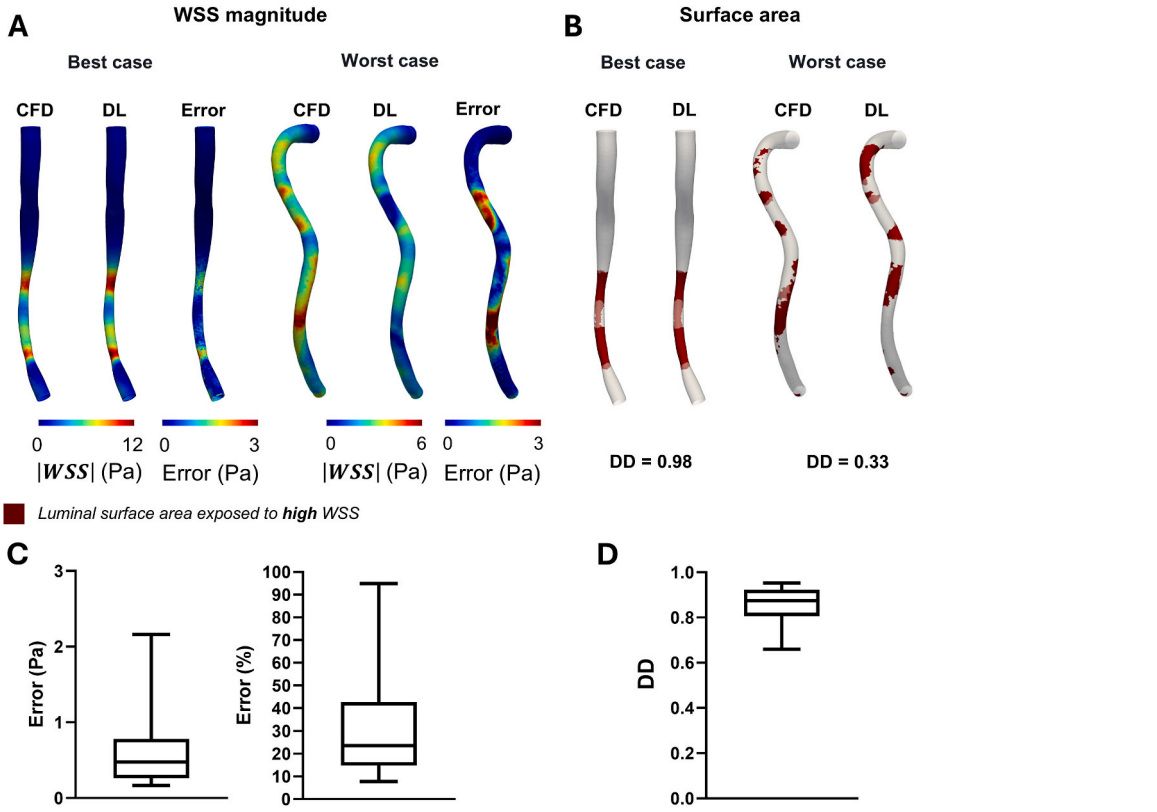

Fig. 4. A. Luminal distribution of WSS magnitude for both CFD and DL with the corresponding error for the best (left) and worst (right) case (left) in terms of DD in the test set obtained with the random split; **B.** Luminal surface areas exposed to high WSS magnitude values mapped on the surface of the vessels; **C.** Boxplot of the surface averaged absolute (left) and percentage (right) errors distributions across the test set; **D.** Boxplot of the DD distribution across the test set. The results refer to the analysis conducted on the held-out test set obtained with the random split of the whole dataset. For the boxplots, the range between the 5th and the 95th percentiles is shown.

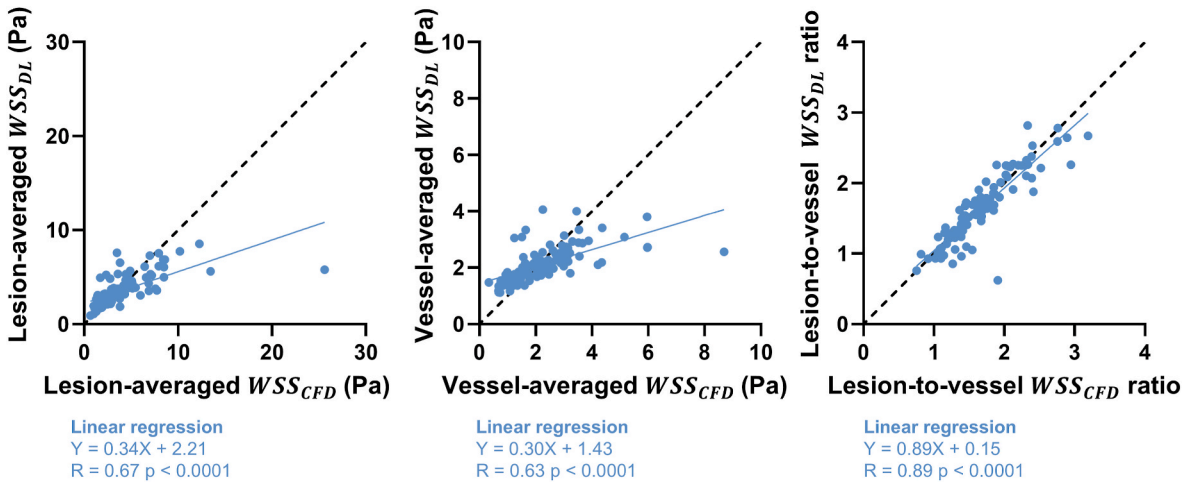

Fig. 5. Lesion-averaged WSS calculated through CFD *vs.* predicted by the DL model with the corresponding linear regression (left panel); vessel-averaged WSS calculated through CFD *vs.* predicted by the DL model with the corresponding linear regression (middle panel); Lesion-to-vessel WSS ratio calculated through CFD *vs.* predicted by the DL model with the corresponding linear regression (right panel). The results refer to the analysis conducted on the held-out test set obtained with the random split of the whole dataset.

considering the lesion-to-vessel WSS ratio (Fig. 5, right panel), normalization of lesion-averaged WSS by vessel-averaged WSS substantially improved the agreement between CFD-derived and GEM-GCN-predicted values ($R = 0.89$, $p < 0.0001$).

Results from the 10-folds cross validation are summarized in Fig. 6. No statistically significant differences were observed across folds for

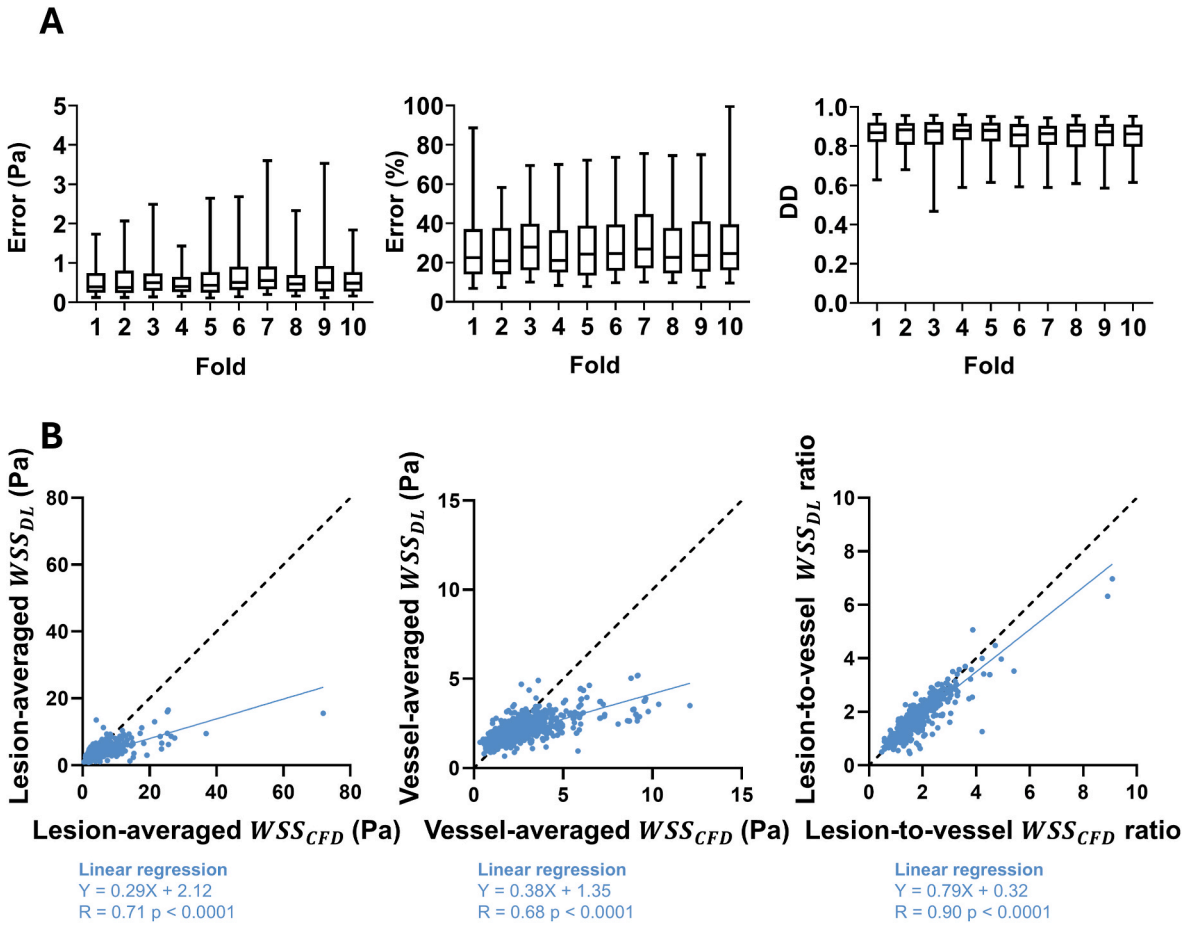

Fig. 6. **A.** Boxplots of the surface-averaged absolute error (left panel), surface-averaged percentage error (middle panel) and DD (right panel); **B.** Lesion-averaged WSS calculated through CFD *vs.* predicted by the DL model with the corresponding linear regression (left panel); vessel-averaged WSS calculated through CFD *vs.* predicted by the DL model with the corresponding linear regression (middle panel); lesion-to-vessel WSS ratio calculated through CFD *vs.* predicted by the DL model with the corresponding linear regression (right panel). The results refer to the 10-fold cross-validation analysis and are obtained aggregating the results from all the 10 held-out test-sets. For the boxplots, the range between the 5th and the 95th percentiles is shown.

surface-averaged absolute error (p = 0.06), surface-averaged percentage error (p = 0.25), and DD (p = 0.50), indicating stable model performance. Aggregating the results from all folds confirmed the trends observed in the random split. Specifically, both lesion-averaged (R = 0.71, p < 0.0001) and vessel-averaged WSS (R = 0.68, p < 0.0001) reaffirmed the moderate discrepancy and the network's systematic underestimation of WSS magnitudes. However, normalization by the vessel-averaged WSS again improved agreement, with the lesion-to-vessel WSS ratio showing strong correlation between GEM-GCN predictions and CFD-derived values (R = 0.90, p < 0.0001).

3.2. External validation with the clinical split analysis and MI risk prediction

This section reports the results referring to the *clinical split* analysis, conducted on the held-out test set comprising all vessels from the multicenter study in Ref. [8]. Fig. 7A illustrates the CFD-derived and GEM-GCN–predicted WSS magnitudes and their corresponding error distributions on the luminal surface for two representative vessels, *i.e.*, the best-performing case (DD = 0.97) and the worst-performing case (DD = 0.32). The corresponding SAs identified by CFD and GEM-GCN for these vessels are shown in Fig. 7B. The overall distribution of surface-averaged WSS magnitude errors across the test samples is shown in Fig. 7C, reported as absolute error (0.65 [0.41-1.12] Pa) and percentage error (29.45 [20.85-45.60]%). These findings are consistent with those obtained from the random split and 10-fold cross validation analyses. As shown in Fig. 7D, the DD confirmed overall co-localization of SAs exposed to elevated WSS magnitudes (DD = 0.84 [0.71-0.90]), indicating strong agreement between CFD and GEM-GCN in identifying luminal regions subjected to high WSS.

Analysis of lesion-averaged WSS (Fig. 8A, R = 0.77, p < 0.0001) and vessel-averaged WSS (Fig. 8A, R = 0.70, p < 0.0001) across the test set vessels confirmed the trends observed in the random split analysis. Consistent with results on the random split of the entire dataset, normalizing lesion-averaged WSS by vessel-averaged WSS substantially improved agreement between CFD-derived and GEM-GCN-predicted values (Fig. 8A, R = 0.91, p < 0.0001).

The predictive performance for future MI was evaluated using ROC curve analysis for both lesion-averaged WSS (Fig. 8B, left panel) and the lesion-to-vessel WSS ratio (Fig. 8B, right panel). Lesion-averaged WSS demonstrated comparable predictive capability for CFD and GEM-GCM, with AUC = 0.63 (95% CI 0.55-0.71, p = 0.0019) and AUC = 0.63 (95% CI 0.55-0.71, p = 0.0034), respectively. No significant difference was observed between the two approaches (DeLong test: p = 0.84). Similar results were obtained for the lesion-to-vessel WSS ratio, with AUC = 0.66 (95% CI 0.58-0.74, p = 0.0002) for CFD, and AUC = 0.68 (95% CI 0.60-0.76, p < 0.0001) for GEM-GCN, with no significant difference between the two approaches (DeLong test: p = 0.37). These findings demonstrate that GEM-GCN-based WSS predictions achieve MI risk prediction capacity comparable to that of CFD-derived WSS, both for lesion-averaged WSS and for the lesion-to-vessel WSS ratio.

4. Discussion

The present study investigated the feasibility of employing a geometric DL-based approach to reliably estimate WSS on the luminal surface of real-world diseased coronary artery models reconstructed from 3D-QCA [8,24,25]. Although the vast majority of studies have reported promising accuracy in coronary WSS estimation using DL-based methods, most rely on synthetic or idealized vascular models

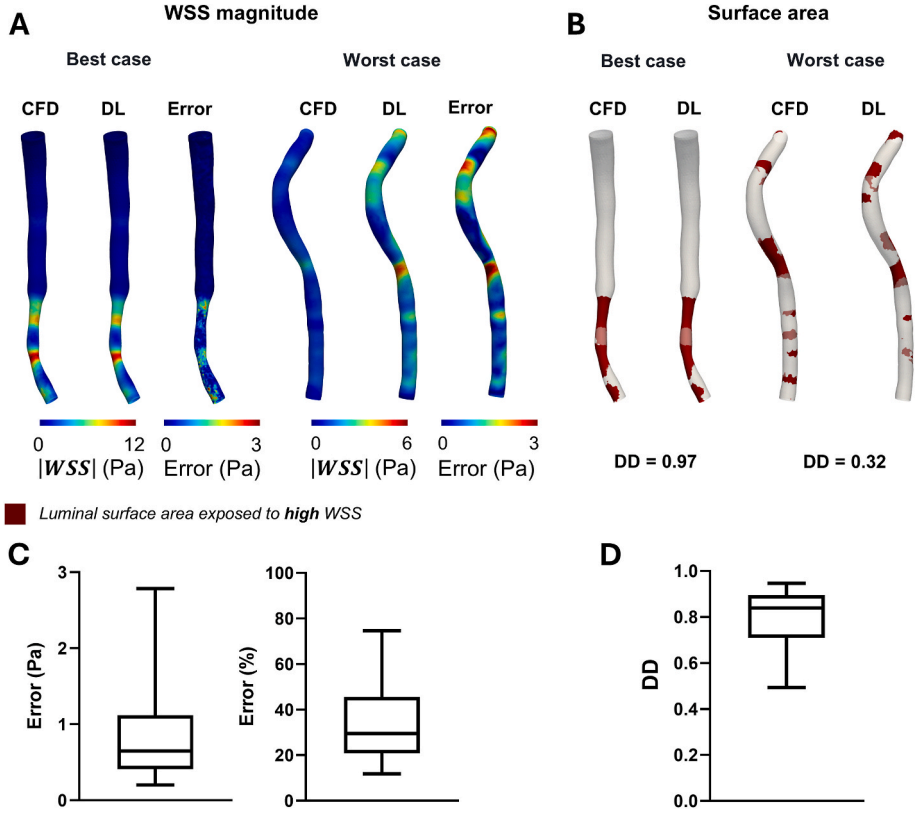

Fig. 7. A. Luminal distribution of WSS magnitude for both CFD and DL with the corresponding error for the best (left) and worst (right) case (left) in terms of DD in the test set obtained with the *clinical split*; **B.** Luminal surface areas exposed to high WSS magnitude values mapped on the surface of the vessels; **C.** Boxplot of the surface averaged absolute (left) and percentage (right) errors distributions across the test set; **D.** Boxplot of the DD distribution across the test set. The results refer to the analysis conducted on the held-out test set comprising all vessels belonging to the *future culprit* population. For the boxplots, the range between the 5th and the 95th percentiles is shown.

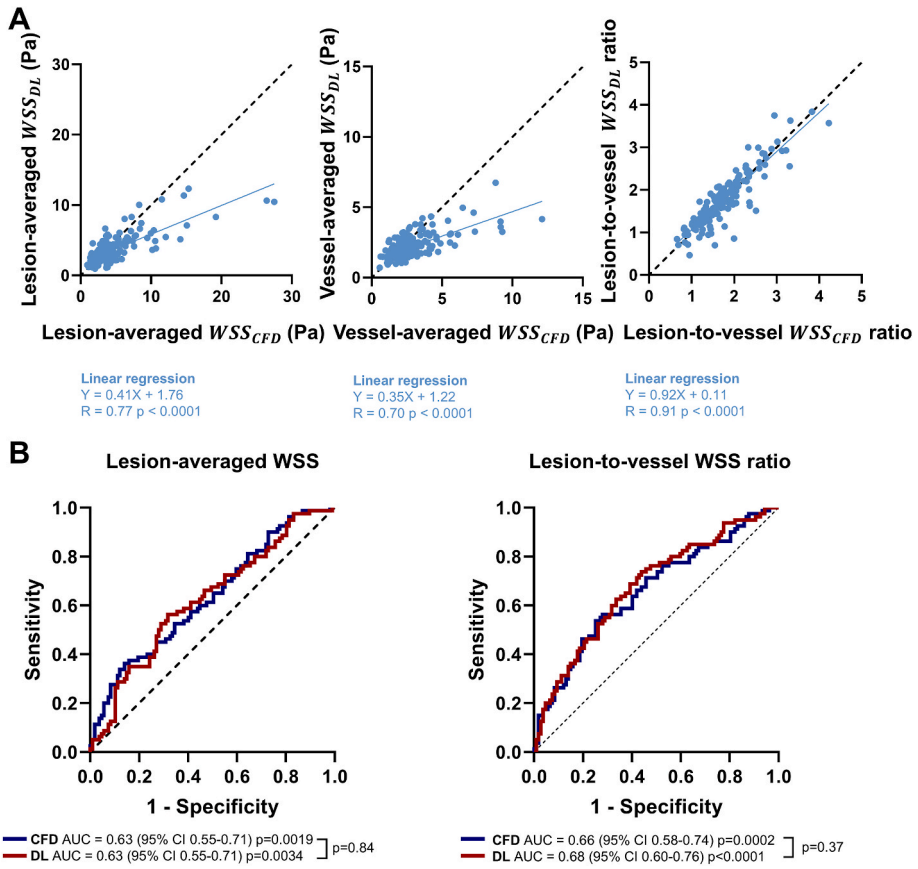

Fig. 8. A. Lesion-averaged WSS calculated through CFD *vs.* predicted by the DL model with the corresponding linear regression (left panel); vessel-averaged WSS calculated through CFD *vs.* predicted by the DL model with the corresponding linear regression (middle panel); lesion-to-vessel WSS ratio calculated through CFD *vs.* predicted by the DL model with the corresponding linear regression (right panel). The results refer to the analysis conducted on the held-out test set comprising all vessels belonging to the *future culprit* population obtained with the *clinical split*. **B)** ROC curves corresponding to the lesion average (left panel) and to the lesion-to-vessel WSS ratio (right panel) for both CFD and DL.

[17–23]. This reliance limits their applicability to clinically derived geometries from real-world patients and limits their generalizability and translational potential.

Addressing these limitations, this study demonstrates that the geometric DL-based framework can effectively capture the near-wall hemodynamics induced by the anatomical complexity of real patient-specific coronary arteries while substantially reducing the computational time required for WSS derivation from personalized CFD simulations.

The adopted approach, based on the GEM-GCN framework, offers several advantages. First, it operates directly on the CFD surface mesh, eliminating the need for vessel parametrization. Second, it is equivariant to rotation and translation [22,30], a property that addresses the absence of a canonical coordinate system in real-world coronary 3D reconstructions.

The main findings of this study can be summarized as follows: (i) the GEM-GCN approach effectively identified coronary luminal surface areas exposed to elevated WSS values; (ii) although GEM-GCN systematically underestimated WSS magnitude relative to CFD, normalization of lesion-averaged WSS by vessel-averaged WSS substantially improved predictive performance; (iii) cross-validation confirmed the stability of the DL model, demonstrating independence from the training samples (no significant differences across ten folds were observed for any of the evaluated metrics); (iv) GEM-GCN-predicted WSS demonstrated predictive capacity for MI at 5 years comparable to that of CFD-derived WSS in an external dataset.

As expected, the GEM-GCN approach exhibited higher errors in patient-specific coronary models compared with those reported for idealized geometries in a previous study (median percentage error: 23.6% *vs.* 7.6% [22]). This discrepancy likely reflects the increased geometric complexity and variability inherent to real-world coronary anatomy. Moreover, our dataset of 1078 image-based coronary geometries is approximately half the size of the dataset used in that study [22] (2000 idealized coronary geometries). Despite these considerations, the adopted DL framework effectively identified luminal SAs exposed to elevated WSS. This finding holds important clinical relevance, given the established role of elevated WSS in the pathophysiological processes underlying plaque progression towards clinical events [3,6,8,9,14]. Overall, the proposed approach demonstrates the potential for fast and accurate identification of vessel regions at increased risk of future MI [8].

Lesion-averaged WSS was analyzed due to its established association with acute coronary events such as future MI [8]. Overall, a moderate linear correlation was observed between GEM-GCN-predicted and CFD-derived WSS values, with a systematic underestimation of WSS magnitude by the DL network (Fig. 5). Similar trends were observed when WSS was averaged over the entire vessel. There was no evidence that stenosis severity affected the considered performance metrics (Fig. S3 of the Supplementary Material). Notably, normalization of lesion-averaged WSS by vessel-averaged WSS substantially improved agreement between CFD-derived and GEM-GCN-predicted values. This improvement can be attributed to the fact that the lesion-to-vessel WSS ratio provides a physically interpretable measure of the relative deviation of WSS within the lesion compared with the WSS distribution across the entire vessel. Specifically, this ratio accentuates local variations in WSS patterns induced by the presence of a lesion relative to the overall

hemodynamic environment, thereby highlighting deviations from the more physiological WSS observed in non-diseased vessel segments. As a normalized quantity, the lesion-to-vessel WSS ratio is also expected to exhibit reduced sensitivity to inflow boundary conditions applied in CFD simulations [37,38], further enhancing the robustness and generalizability of the approach.

Because the proposed DL-based approach is entirely data-driven, assessing its dependence on the training set was essential. To this end, model robustness was evaluated through 10-fold cross-validation. The results confirmed the stable performance of the GEM-GCN, demonstrating consistent identification of luminal SAs exposed to elevated WSS, independent of the specific training samples. This robustness was further corroborated by the strong agreement between results obtained with the random split of the entire dataset and with external validation conducted using the *clinical split*.

Given the established role of WSS in predicting adverse cardiovascular events [6,8,9,14], the *clinical split* enabled evaluation of DL-based WSS capacity as a clinical predictor of MI at 5 years. Remarkably, GEM-GCN-predicted WSS demonstrated predictive capacity comparable to CFD-derived WSS while requiring a computational time of only few seconds per vessel. The moderate predictive power observed in this study is primarily attributable to the multifactorial nature of MI [39]. WSS represents an individual component within a complex pathophysiologic process involving several other concurrent factors. Despite this, our findings underscore the clinical potential of the DL-based framework, which enables rapid WSS estimation without compromising its ability to predict adverse clinical outcomes. Overall, the reported results demonstrate the clinical effectiveness of GEM-GCN-predicted WSS. Specifically, the robustness of performance stability, observed through 10-fold cross-validation and *clinical split*, combined with the ability to identify high-risk regions and the demonstrated predictive power for MI, indicate that the GEM-GCN trained on real-world coronary arteries can rapidly estimate WSS on new geometries, directly derived from 3D-QCA. As 3D-QCA is already part of the standard clinical routine, this approach offers to interventional cardiology valuable biomechanical insights for wider and more informed decision-making in the management of CAD, with minimal additional efforts.

Several limitations of this study should be acknowledged. As previously mentioned, some discrepancies between CFD and DL in terms of WSS magnitude field emerged. This is likely due to the size of the dataset available for this study with respect to the geometrical complexity and inter-individual variability (lesion location along the vessel, number of lesions, vessels' length, and different tortuosity) characterizing vessels derived from real-world patients. The adopted DL model architecture was obtained in prior work [22], where the network hyperparameters were optimized on a dataset of 2000 idealized coronary arteries. The rationale for this choice was to test the translatability of the DL model from ideal to real-world patients. Additionally, the DL model used in this study was trained to predict WSS vector field values averaged over the entire cardiac cycle. Extending the framework to predict WSS at each time step of the cardiac cycle could provide additional clinical and methodological insights. However, previous research has demonstrated that stationary flow conditions, corresponding to cycle-averaged inlet flow rates in coronary arteries, are sufficiently representative of the cycle-averaged WSS magnitude observed under pulsatile flow conditions [37].

In conclusion, this study employed a geometric DL-based approach, GEM-GCN, to estimate WSS on the luminal surface of 3D reconstructed, diseased coronary artery geometries from real-world patients, achieving results within seconds. The proposed framework demonstrated encouraging results with translational potential, particularly in: (i) identifying luminal surface areas exposed to elevated WSS, (ii) quantifying deviations of lesion-specific WSS relative to vessel values, and (iii) providing predictive capacity for future MI risk comparable to CFD simulations. Additional strategies to be explored in future work to reduce these differences include the use of larger datasets, although this remains challenging due to the limited availability of real-world patient data, the implementation of adaptive neighborhood weighting *via* self-attention mechanisms [23,40,41], the explicit encoding of boundary conditions or the incorporation of physical constraints into the loss function [42].

Although further investigation is required before widespread clinical implementation, adopting a geometric DL framework represents a promising and efficient alternative to CFD. By requiring minimal computational time and cost, this approach may ultimately facilitate the integration of WSS assessment into routine interventional cardiology practice.

CRediT authorship contribution statement

Bianca Griffo: Writing – original draft, Visualization, Software, Methodology, Investigation, Formal analysis, Data curation, Conceptualization. **Diego Gallo:** Writing – review & editing, Writing – original draft, Supervision, Methodology, Investigation, Formal analysis, Conceptualization. **David Marlevi:** Writing – review & editing, Supervision, Resources, Methodology, Investigation, Formal analysis. **Marco Laudato:** Writing – review & editing, Supervision, Resources, Methodology, Investigation, Formal analysis. **Girolamo Mastronuzzi:** Writing – review & editing, Formal analysis. **Claudio Chiastra:** Writing – review & editing. **Alessandro Candreva:** Writing – review & editing, Data curation. **Carlos Collet:** Writing – review & editing, Data curation. **Bernard De Bruyne:** Writing – review & editing, Data curation. **Andrea Erriquez:** Writing – review & editing, Data curation. **Gianluca Campo:** Writing – review & editing, Data curation. **Simone Biscaglia:** Writing – review & editing, Data curation. **Umberto Morbiducci:** Writing – review & editing, Writing – original draft, Supervision, Resources, Project administration, Investigation, Funding acquisition, Conceptualization. **Maurizio Lodi Rizzini:** Writing – original draft, Visualization, Supervision, Software, Methodology, Investigation, Formal analysis, Data curation, Conceptualization.

Declaration of generative AI and AI-assisted technologies in the manuscript preparation process

During the preparation of this work the author(s) used ChatGPT (OpenAI) in order to improve manuscript readability. After using this tool/service, the author(s) reviewed and edited the content as needed and take(s) full responsibility for the content of the published article.

Ethics statement

All three datasets analyzed in this work derived from clinical studies conducted in accordance with the ethical principles of the 1975 Declaration of Helsinki, with protocols approved by the respective institutional ethics committees. Written informed consent was obtained from all the enrolled patients.

Declaration of competing interest

DG, **UM**, and **MLR** have received a research grant from Pie Medical Imaging. **AC** has consultancy agreements with Medyria AG and Nanoflex AG. **CCo** reports receiving research grants from Biosensors, Coroventis Research, Medis Medical Imaging, Pie Medical Imaging, CathWorks, Boston Scientific, Siemens, HeartFlow and Abbott Vascular; and consultancy fees from HeartFlow, OpSens Medical, Abbott Vascular and Philips Volcano, and has patents pending on diagnostic methods for coronary artery disease. **BDB** reports receiving consultancy fees from Boston Scientific and Abbott and research grants from Coroventis Research, Pie Medical Imaging, CathWorks, Boston Scientific, Siemens, HeartFlow, and Abbott Vascular. **GC** received grants for research from Sahajanand Medical Technologies, Medis Medical Imaging, Abbott Vascular, GADA, and Siemens Healthineers, outside the present work.

SB received grants for research from Sahajanand Medical Technologies, Medis Medical Imaging, and Siemens Healthineers, outside the present work. The remaining authors have nothing to disclose.

Acknowledgements

This work is part of the project PNRR-NGEU, which has received funding from the MUR – DM 352/2022. DM acknowledges funding from the European Union, ERC, under Grant 101075494, MultiPRESS.

Appendix A. Supplementary data

Supplementary data to this article can be found online at https://doi.org/10.1016/j.compbiomed.2026.111583.

References

[1] S.S. Martin, A.W. Aday, N.B. Allen, Z.I. Almarzooq, C.A.M. Anderson, P. Arora, et al., Heart disease and stroke statistics: a report of US and global data from the American heart association, Circulation 151 (2025), https://doi.org/10.1161/CIR.0000000000001303, 2025.
[2] R. Vergallo, S.-J. Park, G.W. Stone, D. Erlinge, I. Porto, R. Waksman, et al., Vulnerable or high-risk plaque, JACC, Cardiovasc. Imaging 18 (2025) 709–740, https://doi.org/10.1016/j.jcmg.2024.12.004.
[3] R. Vergallo, I.-K. Jang, F. Crea, New prediction tools and treatment for ACS patients with plaque erosion, Atherosclerosis 318 (2021) 45–51, https://doi.org/10.1016/j.atherosclerosis.2020.10.016.
[4] Nisco G. De, E.M.J. Hartman, E. Torta, J. Daemen, C. Chiastra, D. Gallo, et al., Predicting lipid-rich plaque progression in coronary arteries using multimodal imaging and wall shear stress signatures, Arterioscler. Thromb. Vasc. Biol. 44 (2024) 976–986, https://doi.org/10.1161/ATVBAHA.123.320337.
[5] H. Samady, P. Eshtehardi, M.C. McDaniel, J. Suo, S.S. Dhawan, C. Maynard, et al., Coronary artery wall shear stress is associated with progression and transformation of atherosclerotic plaque and arterial remodeling in patients with coronary artery disease, Circulation 124 (2011) 779–788, https://doi.org/10.1161/CIRCULATIONAHA.111.021824.
[6] A. Kumar, E.W. Thompson, A. Lefieux, D.S. Molony, E.L. Davis, N. Chand, et al., High coronary shear stress in patients with coronary artery disease predicts myocardial infarction, J. Am. Coll. Cardiol. 72 (2018) 1926–1935, https://doi.org/10.1016/j.jacc.2018.07.075.
[7] A. Kumar, O.Y. Hung, M. Piccinelli, P. Eshtehardi, M.T. Corban, D. Sternheim, et al., Low coronary wall shear stress is associated with severe endothelial dysfunction in patients with nonobstructive coronary artery disease, JACC Cardiovasc. Interv. 11 (2018) 2072–2080, https://doi.org/10.1016/j.jcin.2018.07.004.
[8] A. Candreva, M. Pagnoni, M.L. Rizzini, T. Mizukami, E. Gallinoro, V. Mazzi, et al., Risk of myocardial infarction based on endothelial shear stress analysis using coronary angiography, Atherosclerosis 342 (2022) 28–35, https://doi.org/10.1016/j.atherosclerosis.2021.11.010.
[9] V. Tufaro, H. Safi, R. Torii, B.-K. Koo, P. Kitslaar, A. Ramasamy, et al., Wall shear stress estimated by 3D-QCA can predict cardiovascular events in lesions with borderline negative fractional flow reserve, Atherosclerosis 322 (2021) 24–30, https://doi.org/10.1016/j.atherosclerosis.2021.02.018.
[10] F. Gijsen, Y. Katagiri, P. Barlis, C. Bourantas, C. Collet, U. Coskun, et al., Expert recommendations on the assessment of wall shear stress in human coronary arteries: existing methodologies, technical considerations, and clinical applications, Eur. Heart J. 40 (2019) 3421–3433, https://doi.org/10.1093/eurheartj/ehz551.
[11] A. Candreva, G. De Nisco, M. Lodi Rizzini, F. D'Ascenzo, G.M. De Ferrari, D. Gallo, et al., Current and future applications of computational fluid dynamics in coronary artery disease, Rev. Cardiovasc. Med. 23 (2022) 377, https://doi.org/10.31083/j.rcm2311377.
[12] P.H. Stone, S. Saito, S. Takahashi, Y. Makita, S. Nakamura, T. Kawasaki, et al., Prediction of progression of coronary artery disease and clinical outcomes using vascular profiling of endothelial shear stress and arterial plaque characteristics: the PREDICTION study, Circulation 126 (2012) 172–181, https://doi.org/10.1161/CIRCULATIONAHA.112.096438.
[13] P.H. Stone, A. Maehara, A.U. Coskun, C.C. Maynard, M. Zaromytidou, G. Siasos, et al., Role of low endothelial shear stress and plaque characteristics in the prediction of nonculprit major adverse cardiac events, JACC, Cardiovasc. Imaging 11 (2018) 462–471, https://doi.org/10.1016/j.jcmg.2017.01.031.
[14] V. Thondapu, C. Mamon, E.K.W. Poon, O. Kurihara, H.O. Kim, M. Russo, et al., High spatial endothelial shear stress gradient independently predicts site of acute coronary plaque rupture and erosion, Cardiovasc. Res. 117 (2021) 1974–1985, https://doi.org/10.1093/cvr/cvaa251.
[15] C. Chiastra, M. Zuin, G. Rigatelli, F. D'Ascenzo, G.M. De Ferrari, C. Collet, et al., Computational fluid dynamics as supporting technology for coronary artery disease diagnosis and treatment: an international survey, Front. Cardiovasc. Med. 10 (2023), https://doi.org/10.3389/fcvm.2023.1216796.
[16] A. Arzani, J.X. Wang, M.S. Sacks, S.C. Shadden, Machine learning for cardiovascular biomechanics modeling: challenges and beyond, Ann. Biomed. Eng. 50 (2022) 615–627, https://doi.org/10.1007/s10439-022-02967-4.
[17] B. Su, J.M. Zhang, H. Zou, D. Ghista, T.T. Le, C. Chin, Generating wall shear stress for coronary artery in real-time using neural networks: feasibility and initial results based on idealized models, Comput. Biol. Med. 126 (2020), https://doi.org/10.1016/j.compbiomed.2020.104038.
[18] R. Gharleghi, A. Sowmya, S. Beier, Transient wall shear stress estimation in coronary bifurcations using convolutional neural networks, Comput. Methods Progr. Biomed. 225 (2022), https://doi.org/10.1016/j.cmpb.2022.107013.
[19] S.H. Alamir, V. Tufaro, M. Trilli, P. Kitslaar, A. Mathur, A. Baumbach, et al., Rapid prediction of wall shear stress in stenosed coronary arteries based on deep learning, Front. Bioeng. Biotechnol. 12 (2024) 1360330, https://doi.org/10.3389/fbioe.2024.1360330.
[20] M. Nikpour, A. Mohebbi, Predicting coronary artery occlusion risk from noninvasive images by combining CFD-FSI, cGAN and CNN, Sci. Rep. 14 (2024) 22693, https://doi.org/10.1038/s41598-024-73396-7.
[21] M.H. Sarkhosh, H. Edrisnia, M.R. Raveshi, M. Sharbatdar, Prediction of time averaged wall shear stress distribution in coronary arteries' bifurcation varying in morphological features via deep learning, Front. Physiol. 16 (2025) 1518732, https://doi.org/10.3389/fphys.2025.1518732.
[22] J. Suk, P. De Haan, P. Lippe, C. Brune, J.M. Wolterink, Mesh neural networks for SE (3)-equivariant hemodynamics estimation on the artery wall, Comput. Biol. Med. 173 (2024) 108328, https://doi.org/10.1016/j.compbiomed.2024.108328.
[23] J. Suk, B. Imre, J.M. Wolterink, LaB-GATr: geometric algebra transformers for large biomedical surface and volume meshes, in: M.G. Linguraru, Q. Dou, A. Feragen, S. Giannarou, B. Glocker, K. Lekadir, et al. (Eds.), Med. Image Comput. Comput. Assist. Interv. – MICCAI 2024, vol 15012, Springer Nature Switzerland, Cham, 2024, pp. 185–195, https://doi.org/10.1007/978-3-031-72390-2_18.
[24] B. De Bruyne, N.H.J. Pijls, B. Kalesan, E. Barbato, P.A.L. Tonino, Z. Piroth, et al., Fractional flow reserve–guided PCI versus medical therapy in stable coronary disease, N. Engl. J. Med. 367 (2012) 991–1001, https://doi.org/10.1056/NEJMoa1205361.
[25] S. Biscaglia, V. Guiducci, J. Escaned, R. Moreno, V. Lanzilotti, A. Santarelli, et al., Complete or culprit-only PCI in older patients with myocardial infarction, N. Engl. J. Med. 389 (2023) 889–898, https://doi.org/10.1056/NEJMoa2300468.
[26] A. Candreva, U. Morbiducci, A. Erriquez, M.L. Rizzini, K. Calò, F.M. Verardi, et al., Enhanced coronary physiology assessment with endothelial shear stress predicts residual cardiovascular risk in older patients with myocardial infarction, Atherosclerosis 409 (2025) 120476, https://doi.org/10.1016/j.atherosclerosis.2025.120476.
[27] Rizzini M. Lodi, A. Candreva, V. Mazzi, M. Pagnoni, C. Chiastra, J.-P. Aben, et al., Blood flow energy identifies coronary lesions culprit of future myocardial infarction, Ann. Biomed. Eng. 52 (2024) 226–238, https://doi.org/10.1007/s10439-023-03362-3.
[28] A.G. van Der Giessen, H.C. Groen, P.-A. Doriot, P.J. De Feyter, A.F.W. van Der Steen, F.N. Van De Vosse, et al., The influence of boundary conditions on wall shear stress distribution in patients specific coronary trees, J. Biomech. 44 (2011) 1089–1095, https://doi.org/10.1016/j.jbiomech.2011.01.036.
[29] M. Lodi Rizzini, D. Gallo, G. De Nisco, F. D'Ascenzo, C. Chiastra, P.P. Bocchino, et al., Does the inflow velocity profile influence physiologically relevant flow patterns in computational hemodynamic models of left anterior descending coronary artery? Med. Eng. Phys. 82 (2020) 58–69, https://doi.org/10.1016/j.medengphy.2020.07.001.
[30] P. de Haan, M. Weiler, T. Cohen, M. Welling, Gauge equivariant mesh CNNs: anisotropic convolutions on geometric graphs. https://doi.org/10.48550/ARXIV.2003.05425.
[31] K. He, X. Zhang, S. Ren, J. Sun, Deep Residual Learning for Image Recognition, 2015, https://doi.org/10.48550/ARXIV.1512.03385.
[32] J. Gilmer, S.S. Schoenholz, P.F. Riley, O. Vinyals, G.E. Dahl, Neural Message Passing for Quantum Chemistry, 2017, https://doi.org/10.48550/arXiv.1704.01212.
[33] R. Wiersma, E. Eisemann, K. Hildebrandt, CNNs on surfaces using rotation-equivariant features, ACM Trans. Graph. 39 (2020), https://doi.org/10.1145/3386569.3392437.
[34] V. Nair, G.E. Hinton, Rectified linear units improve restricted boltzmann machines, Int. Conf. Mach. Learn. (2010) 807–814, https://doi.org/10.5555/3104322.3104425.
[35] N. Sharp, Y. Soliman, K. Crane, The vector heat method, ACM Trans. Graph. 38 (2019) 1–19, https://doi.org/10.1145/3243651.
[36] E.R. DeLong, D.M. DeLong, D.L. Clarke-Pearson, Comparing the areas under two or more correlated receiver operating characteristic curves: a nonparametric approach, Biometrics 44 (1988) 837, https://doi.org/10.2307/2531595.
[37] M. Lodi Rizzini, A. Candreva, C. Chiastra, E. Gallinoro, K. Calò, F. D'Ascenzo, et al., Modelling coronary flows: impact of differently measured inflow boundary conditions on vessel-specific computational hemodynamic profiles, Comput. Methods Progr. Biomed. 221 (2022) 106882, https://doi.org/10.1016/j.cmpb.2022.106882.
[38] J.T.C. Schrauwen, J.C.V. Schwarz, J.J. Wentzel, A.F.W. Van Der Steen, M. Siebes, F.J.H. Gijsen, The impact of scaled boundary conditions on wall shear stress computations in atherosclerotic human coronary bifurcations, Am. J. Physiol. Heart Circ. Physiol. 310 (2016) H1304–H1312, https://doi.org/10.1152/ajpheart.00896.2015.
[39] M.E. Ahmed, D. Hakim, P.H. Stone, The plaque hypothesis: understanding mechanisms of plaque progression and destabilization, and implications for clinical

management, Curr. Opin. Cardiol. 38 (2023) 496–503, https://doi.org/10.1097/HCO.0000000000001077.

[40] G. Nannini, J. Suk, P. Rygiel, S. Saitta, L. Mariani, R. Maranga, et al., Learning hemodynamic scalar fields on coronary artery meshes: a benchmark of geometric deep learning models, Comput. Biol. Med. 195 (2025) 110477, https://doi.org/10.1016/j.compbiomed.2025.110477.

[41] MdK. Hasan, Y. Luo, G. Yang, C.H. Yap, Feedback attention to enhance unsupervised deep learning image registration in 3D echocardiography, IEEE Trans. Med. Imag. 44 (2025) 2230–2243, https://doi.org/10.1109/tmi.2025.3530501.

[42] X. Zhang, B. Mao, Y. Che, J. Kang, M. Luo, A. Qiao, et al., Physics-informed neural networks (PINNs) for 4D hemodynamics prediction: an investigation of optimal framework based on vascular morphology, Comput. Biol. Med. 164 (2023) 107287, https://doi.org/10.1016/j.compbiomed.2023.107287.